Effect of Cr Content on Hot Corrosion Behavior of Inconel Alloys in Molten LiCl–Li$_2$O

Kyu-Seok Lim[1] · Woo-Seok Choi[1] · Wan-Bae Kim[1] · Soo-Haeng Cho[2] · Jong-Hyeon Lee[1,2,3]

Abstract

The hot corrosion behaviors of Inconel alloys with different Cr contents (Inconel 600, 601, and 690), which are used widely in nuclear plants, were investigated in molten LiCl–Li$_2$O salts. The hot corrosion behaviors were studied by measuring the mass and attack depth changes, surface and cross-sectional morphologies and elemental distributions, and compositional changes at the subscale and substrate scale as well as the spalled oxide scale. At 288 h, the weight losses of Inconel 601 and Inconel 690 were approximately four and twelve times higher, respectively, than that of Inconel 600. The corrosion products of all tested alloys were Cr$_2$O$_3$, NiO, and FeCr$_2$O$_4$. Inconel 600, which exhibited a dense and continuous external corrosion layer and an internal corrosion layer with localized corrosion behavior, exhibited superior corrosion resistance compared with those of Inconel 601 and 690, which showed a spalled external corrosion layer and an internal corrosion layer with uniform corrosion behavior. Thus, the corrosion resistance of the Inconel alloys tested in the hot lithium molten salts in an oxidizing atmosphere is closely related to the contents of the primary alloying elements in the alloys. Of the various alloys analyzed in this study, Inconel 600 exhibited the highest corrosion resistance. Thus, a Cr content of 16.30 wt% or less, Ni content of at least 73.66 wt%, and Fe content considerably lower than 8.15 wt% can result in excellent corrosion resistance.

Keywords Hot corrosion behavior · Alloying elements · Chromium content · Chromium depletion · Electrochemical reduction

✉ Jong-Hyeon Lee
jonglee@cnu.ac.kr

1 Department of Materials Science and Engineering, Chungnam National University, Daejeon 34134, Korea

2 Rapidly Solidified Materials Research Center (RASOM), Chungnam National University, Daejeon 34134, Korea

3 Graduate School of Energy Science and Technology, Chungnam National University, Daejeon 34134, Korea

Introduction

Electrolytic reduction using molten salts as the reaction medium is a key technology for reducing metal oxides to their metallic forms. Molten salts have recently attracted considerable research attention for use in industrial applications, such as energy storage [1–3], metal refinement [4–6], and fuel cells [7–9]. This is because of their physicochemical properties such as their high electrical conductivity, high processing rate, and fluid-like characteristics. However, these salts can corrode the various components of the electrolysis equipment, such as the reactor. Therefore, the long-term corrosion resistance of materials is an important parameter for determining their suitability for use in structural applications that require continuous exposure to molten salts. Thus far, many studies have focused on the hot corrosion behavior of Ni-based alloys used for fabricating the equipment used to handle molten salts of the chloride [10–14], fluoride [15–18], and carbonate systems [19–23]. In addition, Ni-based alloys are being used in high-temperature applications because of their excellent resistance against corrosion at elevated temperatures [24–40].

During the electrolytic reduction of spent oxide nuclear fuel in molten lithium salts, the oxygen generated at the anode and the hot strongly basic lithium oxide make ordinary structural materials highly susceptible to corrosion [6, 41–45]. Therefore, a suitable structural material is required to handle the molten salts during the electrolytic reduction of the spent oxide nuclear fuel. The hot corrosion behavior of high-temperature materials and their performance in molten lithium salt needs to be characterized. However, there have been only a few studies on the hot corrosion behavior of Ni-base alloys in molten LiCl-Li$_2$O salts [41–45]. According to these studies, the formation, maintenance, and spalling of the external corrosion layer and the shape and growth of the internal corrosion layer as well as the depletion of the major alloying elements beneath the corrosion layer significantly affect the weight loss of the alloy. Many alloys used for high-temperature applications are based on Ni, and they rely on the formation of a Cr$_2$O$_3$ layer for resistance against corrosion. This is because the Cr$_2$O$_3$ layer is thermodynamically stable with respect to the metals involved. However, the effect of the Cr content on the hot corrosion behavior of Inconel alloys, which are widely used in nuclear plants, is yet to be evaluated systematically.

In this study, the effects of the Cr content on the hot corrosion behavior of the Ni-based alloys Inconel 600, Inconel 601, and Inconel 690 were investigated under simulated electrolytic reduction conditions. The mass and attack depth changes as well as the surface and cross-sectional morphologies, characteristics, and elemental distributions of the oxide scales were analyzed.

Experimental Procedures

Specimen Preparation

In this study, we evaluated three Inconel alloys with varying Cr contents: 600 (16.30 wt%), 601 (22.50 wt%), and 690 (29.82 wt%). The chemical compositions of

these alloys are listed in Table 1. The specimens (dimensions: 70 mm (L)×15 mm (W)×2 mm (T)) were ground using SiC paper (#2,000), polished with diamond paste, washed with deionized water, and ultrasonically degreased in ethanol.

Hot Corrosion Testing

A schematic of the hot corrosion testing process is shown in Fig. 1. The experimental setup includes a unit reaction system consisting of a reactor and auxiliary facilities and a mixed-gas supply system with a mixed-gas storage package. As shown in Fig. 1, the apparatus is equipped with three MgO crucibles, each of which held one specimen. Corrosion studies on the samples were repeated three times under the same experimental conditions to improve the accuracy of the examination and secure the reliability of the weight loss, and the average of these results was used as the final weight-loss value. A mixture of as-purchased LiCl (Rare Metallic Co., Ltd., Japan, 99.9%) and Li_2O (Cerac, USA, -100 mesh, 99.5%) powders was used as the molten salt. The mixture was introduced into a high-density MgO crucible and heated at 300 °C for 4 h in an Ar atmosphere to remove all the moisture. The corrosion test was conducted by completely immersing the test alloy in the molten salt in a glove box; the corrosion reaction temperature was 650 °C, exposure time was 24–288 h, Li_2O concentration was 3 wt%, and mixed-gas (Ar-10% O_2) supply rate was 5 mL/min. After the hot corrosion test, the test alloy was separated from the molten salt and kept in an Ar atmosphere in a glove box while the furnace was allowed to cool to room temperature (15–20 °C).

Characterization

After the reactor was opened, the alloy specimens were removed and visually examined before being ultrasonically cleaned with deionized water to remove the molten salt adhering to their surfaces. Subsequently, the specimens were dried at 90 °C for at least 24 h. To assess the extent of corrosion, the initial and final weights of the specimens were measured using an analytical balance (Sartorius QUINTIX224-1S, Germany). The corroded specimens were then cut using a diamond cutter and ultrasonically cleaned with acetone for characterization. The specimens for metallographic examination were prepared by cold mounting, grinding, and polishing. The morphology, microstructure, chemical composition, and elemental distribution of the subscale, substrate, and spallation sections of the oxide scales were examined using field-emission scanning electron microscopy (FE-SEM; JEOL, JSM-7000F) coupled with

Table 1 Chemical compositions of tested alloys (wt%)

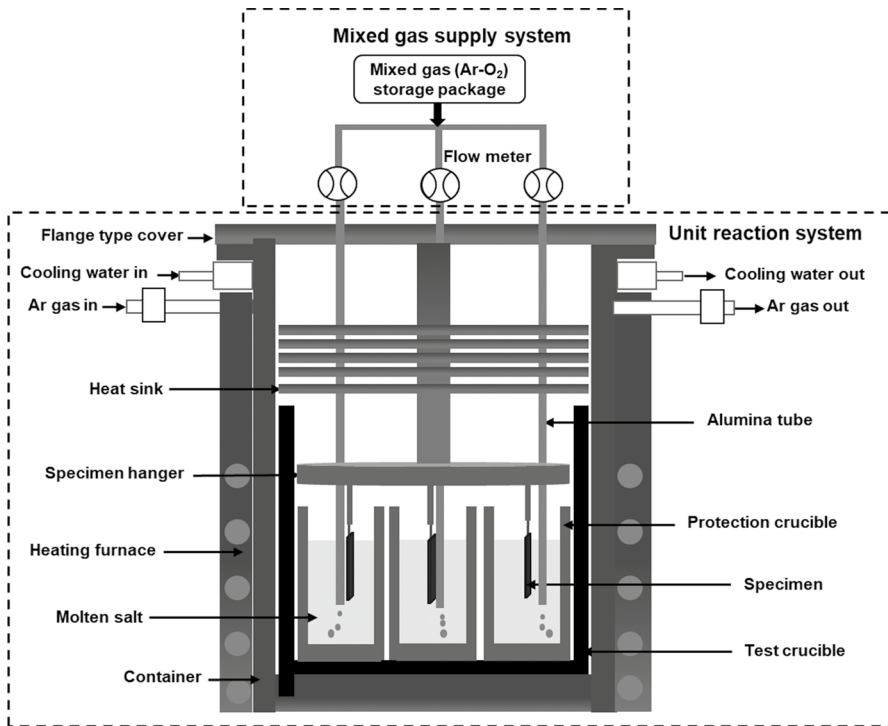| Alloy	Ni	Cr	Fe	C	Mn	P	Al	Cu	Ti
Inconel 600	73.66	16.30	8.15	0.07	0.32	0.002	–	0.05	–
Inconel 601	60.53	22.50	13.0	0.03	0.30	0.002	1.30	0.03	–
Inconel 690	56.30	29.82	10.0	0.08	0.28	0.001	0.32	0.01	0.32

Fig. 1 Schematic of apparatus used for corrosion test

energy dispersive spectroscopy (EDS) using an applied voltage and vacuum pressure of 15 kV and 7.04×10^{-4} Pa, respectively. The phase structures of the corrosion products were determined by X-ray diffraction (XRD) analysis (Rigaku, D/MAX-2200 Ultima/PC), which was performed using Cu-Kα radiation. Scanning was performed over the half-width (2θ) range of 15–100° with a step size of 0.05° and scan rate of 3.5°/min at 40 kV and 40 mA. Thermodynamic calculations were performed using HSC Chemistry 7.1 (Outotec) to confirm the content of the corrosion products at equilibrium [46].

Results and Discussion

Weight Loss

Figure 2 shows the weight losses of the Inconel 600, 601, and 690 specimens corroded at 650 °C in LiCl-3 wt% Li_2O as functions of the exposure time. The Inconel 690 and 600 specimens showed the highest and lowest weight losses, respectively. Further, the weight loss of the Inconel 600 specimen increased more slowly than

those of the Inconel 601 and 690 specimens. The weight loss of the Inconel 600 specimen, which had the lowest Cr content (16.30 wt%), did not significantly vary when the exposure time was lower than 168 h; thereafter, the weight loss increased slightly (Fig. 2). The weight loss of the Inconel 601 specimen, which had a Cr content of 22.50 wt%, was approximately four times higher than that of the Inconel 600 specimen at 288 h. Further, the weight loss of the Inconel 690 specimen, which had the highest Cr content (29.82 wt%), was approximately twelve times higher than that of the Inconel 600 specimen at 288 h (Fig. 2). From the above results, it is evident that the higher the Cr content, the greater the weight loss, which indicates that excessive Cr content inhibits corrosion resistance. That said, this tendency can be significantly affected by the formation, maintenance, and spallation of the corrosion layer. Also, referring to Fig. 2, a gentle slope of the weight loss indicates that the corrosion layer acts as a protective film, while a rapidly increasing slope indicates that the porous corrosion layer does not function as a protective film. This is further detailed in Sect. "Corrosion Behaviors".

Figure 3 shows the attack depths of the Inconel 600, 601, and 690 specimens corroded at 650 °C in the molten salt as functions of the exposure time. As shown in the insets of Fig. 3, the attack depth is the sum of the depths of the external and internal corrosion layers. The attack depths of the Inconel 600 and 601 specimens gradually increased with an increase in the exposure time. In contrast, that of the Inconel 690 specimen increased sharply with the exposure time, particularly after 168 h. Comparing the results of Figs. 2 and 3 revealed that the changes in the weight loss and attack depth over time exhibited similar trends.
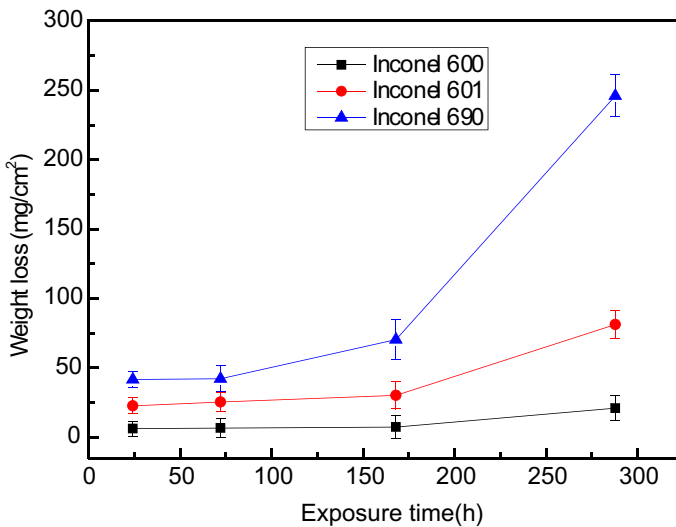

Fig. 2 Weight losses of Inconel 600, 601, and 690 specimens corroded at 650 °C in LiCl-3 wt% Li$_2$O as functions of exposure time
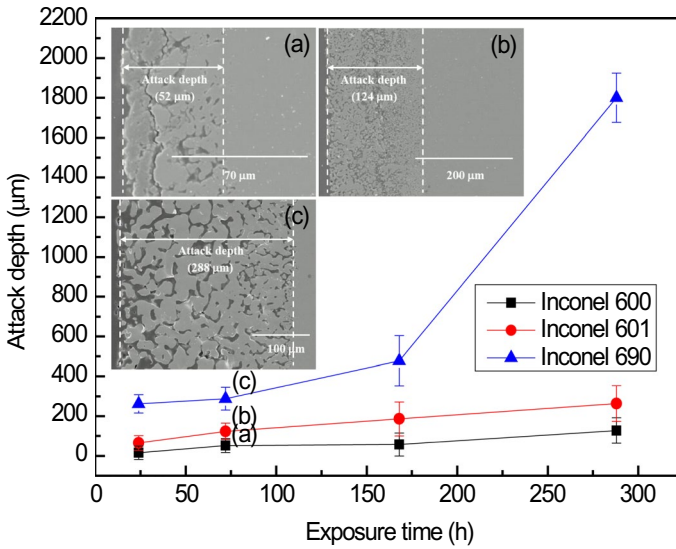
Fig. 3 Attack depths of Inconel 600, 601, and 690 specimens corroded at 650 °C in LiCl-3 wt% Li_2O as functions of exposure time

Hot Corrosion Products

Figures 4, 5 and 6 show the XRD patterns of the corrosion products of the Inconel 600, 601, and 690 specimens corroded at 650 °C in molten LiCl-3 wt% Li_2O for 72–288 h. The corrosion products of all tested specimens were Cr_2O_3, $FeCr_2O_4$, and NiO. From a thermodynamic perspective, Cr_2O_3 is the most stable oxide in Ni/Fe/Cr-based alloys [47]. Thus, Cr_2O_3 was initially formed as a hot corrosion product followed by $FeCr_2O_4$ spinel, which was formed through the following reactions:

Initially, Cr_2O_3 reacted with the O^{2-} ions of Li_2O in the molten salt according to the following reaction:

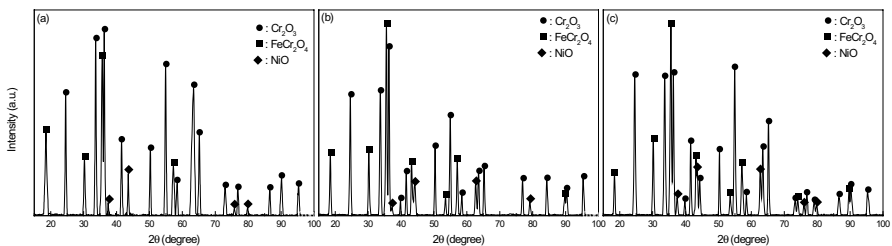$$Cr_2O_3 + O_2^- \rightarrow 2CrO_2^- \tag{1}$$

Fig. 4 X-ray diffraction (XRD) patterns of corrosion products of Inconel 600 specimen corroded at 650 °C for 72 h (**a**), 168 h (**b**), and 288 h (**c**) in LiCl-3 wt% Li_2O
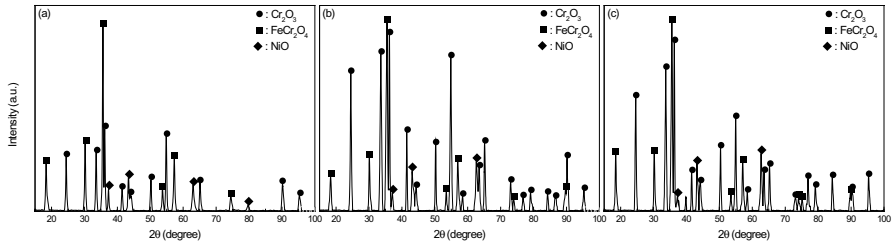
Fig. 5 XRD patterns of corrosion products of Inconel 601 specimen corroded at 650 °C for 72 h (**a**), 168 h (**b**), and 288 h (**c**) in LiCl-3 wt% Li$_2$O
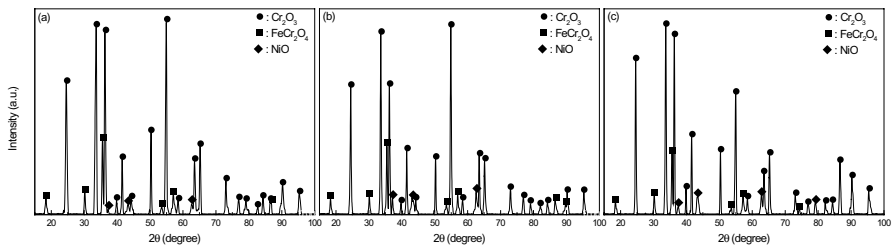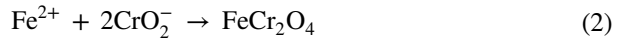

Fig. 6 XRD patterns of corrosion products of Inconel 690 specimen corroded at 650 °C for 72 h (**a**), 168 h (**b**), and 288 h (**c**) in LiCl-3 wt% Li$_2$O

Fe ions diffuse through the initially formed Cr oxide layer and react with CrO_2^- to form spinel-type $FeCr_2O_4$, as shown by the following reaction:

$$Fe^{2+} + 2CrO_2^- \rightarrow FeCr_2O_4 \tag{2}$$

In the case of the Inconel 600 specimen (Fig. 4), the intensity of the Cr_2O_3 peak was slightly higher than that of the $FeCr_2O_4$ peak for 72 h; however, with an increase in the exposure time, the intensity of the $FeCr_2O_4$ peak became slightly higher than that of the Cr_2O_3 peak. Figure 5 shows that, for the Inconel 601 specimen, the intensity of the $FeCr_2O_4$ peak was higher than that of the Cr_2O_3 peak for 72 h; this is because of the high Fe content (13.0 wt%) and the diffusion coefficients of the metal ions in oxides, which can be arranged in the following order: $Fe^{3+} > Fe^{2+} > Ti^{3+} > Ni^{2+} > Cr^{3+}$ [48]. In addition, Fig. 6 shows that, for the Inconel 690 specimen, the intensity of the Cr_2O_3 peak was higher than that of the $FeCr_2O_4$ peak at 72 h because of the selective oxidation of a larger amount of Cr (29.82 wt%). The reason the intensity of the Cr_2O_3 peak in Inconel 690 is greater than that of $FeCr_2O_4$ is believed to be due to the higher growth rate of the Cr_2O_3 layer than the outward diffusion rates of Fe and Ni ions. Thus, the intensity of the corrosion product peak is related to the contents and diffusivities of the alloying elements involved in the formation of the oxide layer.

Figure 7 shows the equilibrium compositions as determined from the thermodynamic calculations based on the compositions of the Inconel 600, 601, and 690 specimens in the LiCl–Li$_2$O–O$_2$ system. The XRD results shown in Figs. 4, 5 and 6

are relatively consistent with the results of these calculations (Inconel 600–Ni: 73.66 wt%, Cr: 16.30 wt%, Fe 8.15 wt%, and Mn: 0.32 wt% (Fig. 7a); Inconel 601–Ni: 60.53 wt%, Cr: 22.50 wt%, Fe 13.00 wt%, and Al: 1.30 wt% (Fig. 7b); and Inconel 690–Ni: 56.30 wt%, Cr: 29.82 wt%, Fe 10.00 wt%, Al: 0.32 wt%, and Ti: 0.32 wt% (Fig. 7c). All the calculations were performed using HSC Chemistry (version 7.1) [46]. In particular, the amounts of products at equilibrium were calculated in the isothermal and isobaric conditions based on the Gibbs energy minimization of components (see Fig. 7). The corrosion test time may not be sufficient to reach the equilibrium condition, but the interpretation is valid because the phases obtained by XRD. The insets in Figs. 7a, b and c show the results of the thermodynamic calculations performed to identify the peaks of the corrosion products because the peaks of $FeCr_2O_4$ and $NiCr_2O_4$ are similar. The calculations indicate that, in the tested alloys, the corrosion product $FeCr_2O_4$ is more stable than $NiCr_2O_4$ (see Eqs. (3) and (4)), which is in good agreement with the results shown in Figs. 4, 5 and 6. The relevant reactions are:
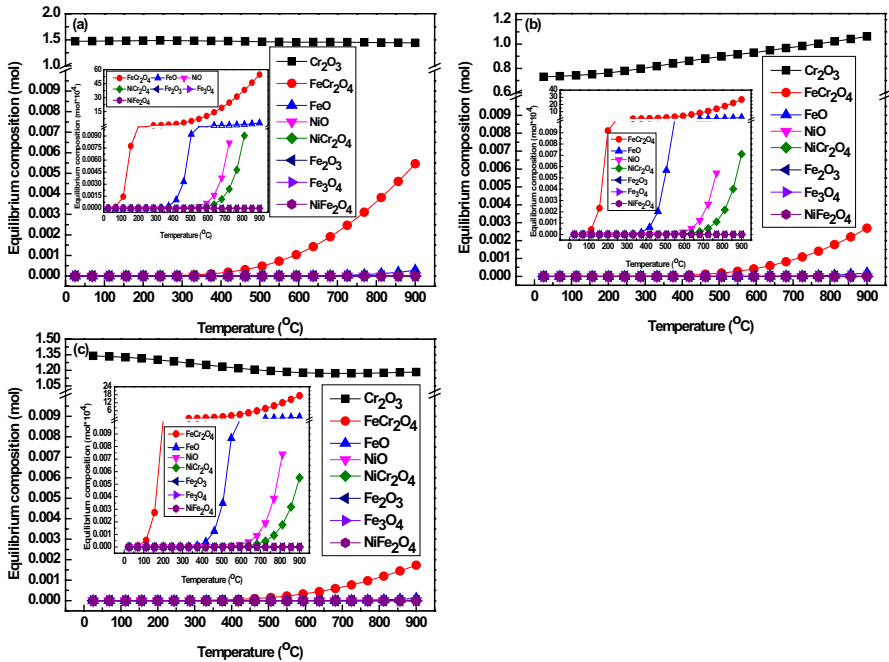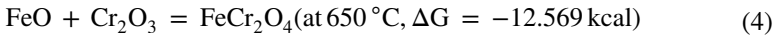
$$NiO + Cr_2O_3 = NiCr_2O_4 \ (at\ 650\,°C,\ \Delta G = -1.638\,kcal) \tag{3}$$

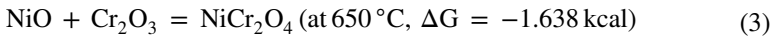$$FeO + Cr_2O_3 = FeCr_2O_4 (at\ 650\,°C,\ \Delta G = -12.569\,kcal) \tag{4}$$

Fig. 7 Calculated equilibrium compositions of Inconel 600 (**a**), 601 (**b**), and 690 (**c**) specimens in LiCl-Li_2O-O_2 system as functions of temperature

Corrosion Behaviors

Figure 8 shows the cross-sectional SEM images of the corrosion layers of the Inconel 600, 601, and 690 specimens corroded at 650 °C in molten LiCl-3 wt% Li_2O for 72 h. As shown in Fig. 8a, the corrosion layer of the Inconel 600 specimen comprises an external corrosion layer with some pores and an internal corrosion layer. In contrast, the external corrosion layers of the Inconel 601 (Fig. 8b) and 690 (Fig. 8c) specimens were spalled, and only an internal corrosion layer with many pores was observed. Further, the internal corrosion behavior of the Inconel 600 specimen was localized, whereas those of the Inconel 601 and 690 specimens showed uniform corrosion. The external corrosion layer of the Inconel 600 specimen was dense and continuous and acted as an effective barrier against the inward diffusion of oxygen ions and the outward diffusion of metal ions in the corrosion environment [49]. The internal corrosion layers of the Inconel 601 and 690 specimens contained cracks and pores, were coarse and discontinuous and acted as an intrusion channel for the molten salts and oxygen during the corrosion process. Therefore, these pores and cracks had a determining effect on the corrosion resistance of the corroded surface layer [50]. The spallation of the oxide layers is likely caused by the differences in the thermal expansion coefficients or the pores at the oxide layer/base metal interface generated because of the increasing internal stress attributed to the formation of the oxide layer [51]. Thus, the external corrosion layer has a considerable influence on the shape and growth of the internal corrosion layer. Based on the aforementioned results, it is believed that the weight loss shown in Fig. 2 can be significantly affected by the maintenance of the external corrosion layer and the formation of the internal corrosion layer.

Figure 9 shows the cross-sectional SEM images, EDS results, and X-ray line scan analysis results for the Inconel 600, 601, and 690 specimens corroded at 650 °C in LiCl-3 wt% Li_2O for 72 h. In the case of the Inconel 600 specimen, the localized EDS analysis and X-ray line scan results shown in Fig. 9a confirm that the external corrosion layer (S1, S2) is rich in Cr, Fe, and O, with a small amount of Ni also present. These elements were present as Cr_2O_3, $FeCr_2O_4$, and NiO, as identified by the XRD analysis and shown in Fig. 4a. The dense Ni-rich phase (S4) beneath the external corrosion layer acts as an effective barrier to the inward diffusion of oxygen ions and the outward diffusion of metal ions in the corrosion environment.
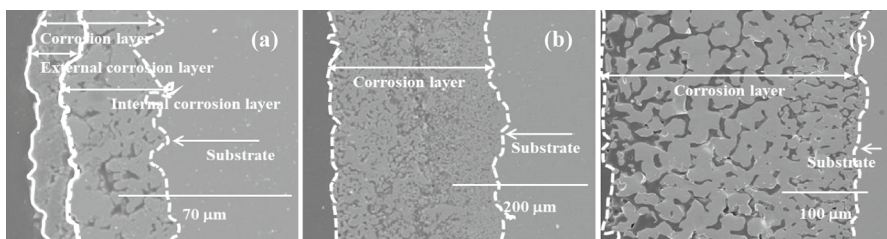

Fig. 8 Cross-sectional SEM images of Inconel 600 (**a**), 601 (**b**), and 690 (**c**) specimens corroded at 650 °C in LiCl-3 wt% Li_2O for 72 h
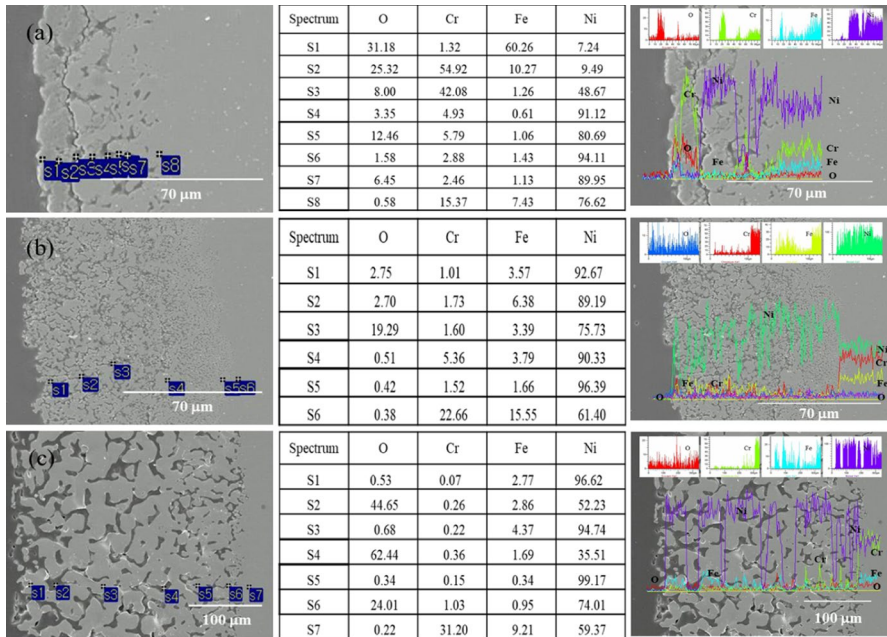
Fig. 9 Cross-sectional SEM images and EDS and X-ray line scan results of Inconel 600 (**a**), 601 (**b**), and 690 (**c**) specimens corroded at 650 °C in LiCl-3 wt% Li_2O for 72 h

(a)

Spectrum	O	Cr	Fe	Ni
S1	31.18	1.32	60.26	7.24
S2	25.32	54.92	10.27	9.49
S3	8.00	42.08	1.26	48.67
S4	3.35	4.93	0.61	91.12
S5	12.46	5.79	1.06	80.69
S6	1.58	2.88	1.43	94.11
S7	6.45	2.46	1.13	89.95
S8	0.58	15.37	7.43	76.62

(b)

Spectrum	O	Cr	Fe	Ni
S1	2.75	1.01	3.57	92.67
S2	2.70	1.73	6.38	89.19
S3	19.29	1.60	3.39	75.73
S4	0.51	5.36	3.79	90.33
S5	0.42	1.52	1.66	96.39
S6	0.38	22.66	15.55	61.40

(c)

Spectrum	O	Cr	Fe	Ni
S1	0.53	0.07	2.77	96.62
S2	44.65	0.26	2.86	52.23
S3	0.68	0.22	4.37	94.74
S4	62.44	0.36	1.69	35.51
S5	0.34	0.15	0.34	99.17
S6	24.01	1.03	0.95	74.01
S7	0.22	31.20	9.21	59.37

The presence of a Ni-rich layer at the oxide layer/oxide layer or oxide layer/base metal interface reduces the oxidation rate of alloys [45]. In addition, the Cr content in the Cr-depleted region of the internal corrosion layer beneath the external corrosion layer of the alloy was 2.46–5.79 wt%; this was attributable to the enrichment of Cr in the external corrosion layer (S2 and S3) and the formation of Cr oxides. Ling et al. [52] reported a Cr-depleted region beneath the external Cr_2O_3 layer and hypothesized that this depletion is caused by the consumption of Cr to form oxides on the specimen surface. Further, the depletion of Fe (S3–S7) in the internal corrosion layer was attributable to the enrichment of Fe (S1) in the external corrosion layer and the formation of Fe oxide corrosion products. However, the weight loss of the specimen will be affected when the external corrosion layer undergoes spalling with an increase in exposure time. For the Inconel 601 specimen, the Ni-rich phase (S1) in the outermost layer is discontinuous and coarse and contains cracks and thus cannot act as an effective barrier (Fig. 9b). Thus, the corrosion reaction is expected to accelerate in the internal corrosion layer because the molten salt and oxygen can penetrate the cracks. The localized EDS analysis of the internal corrosion layer showed considerable decreases in the Cr (1.01–5.36 wt%) and Fe (1.66–6.38 wt%) contents. Consequently, the increased depletion of Cr and Fe is expected to further accelerate the kinetics of internal corrosion [53]. In the case of the Inconel 690 specimen, the morphology of the internal corrosion layer was almost similar to that of the Inconel 601 specimen; however, Cr depletion in the outermost layer (S1) was more severe than that in case of the Inconel 601 specimen. The Cr- and Fe-depleted

regions became susceptible to internal corrosion and the formation of a nonprotective Ni-rich phase and/or a Ni-rich oxide when the scale eventually ruptured with continued exposure [49]. The Cr contents of the outermost layers (S1) of the Inconel 601 and 690 specimens were 1.01 wt% and 0.07 wt%, respectively. These results indicated that the high intensity of the Cr_2O_3 peak in Fig. 6a was attributable to the preferential selective oxidation of Cr in the Inconel 690 specimen, which had a high Cr content (29.82 wt%). The above-mentioned descriptions are consistent with the results shown in Figs. 2 and 3.

Figure 10 shows the surface SEM images and EDS and XRD analysis results of the inner and outer surfaces of the spalled Inconel 600 plate corroded in LiCl-3 wt% Li_2O for 168 h. The surface morphology of the inner scales in contact with the substrate (Fig. 10a) consists of irregular polyhedral crystals along with random nodular crystals rich in Cr, Ni, Fe, and O. These crystals were likely of FeO, Cr_2O_3, NiO, $FeCr_2O_4$, and $(Cr, Fe)_2O_3$, based on the XRD analysis results shown in Fig. 10a. Thus, Fe-rich oxides were formed. Fe-rich oxides are less dense than Cr- and Ni-based oxides. Low-density oxides can lead to many cation defects, including pores, internal stress, and hence spallation at the oxide layer/oxide layer and oxide layer/base metal interfaces [54]. Hence, the formation of the Fe-oxide phase can reduce corrosion resistance. The surface morphology of the outer scales in contact with the molten salt, shown in Fig. 10b, consists of irregular nodular crystals with a network structure. These were rich in Cr, Fe, and Ni, suggesting that they were of oxides such as Cr_2O_3, $FeCr_2O_4$, and NiO, based on the XRD analysis (Fig. 10b).
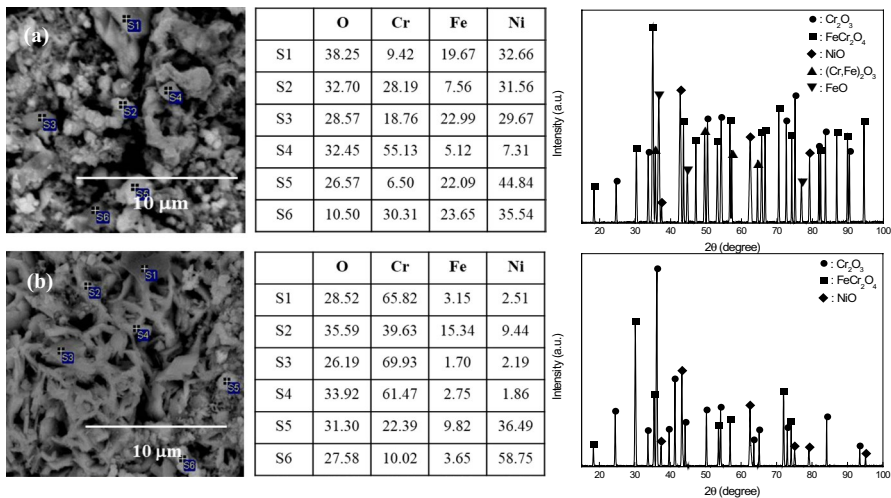

Fig. 10 Surface SEM images and EDS and XRD analysis results of **a** inner and **b** outer surfaces of spalled corrosion plate of Inconel 600 specimen corroded in LiCl-3 wt% Li_2O for 168 h

Conclusions

The hot corrosion behaviors of Inconel alloys with varying Cr contents (i.e., Inconel 600, 601, and 690) were investigated at 650 °C in molten $LiCl$-Li_2O salts. The weight losses and attack depths of the specimens could be arranged as follows: Inconel 600 < Inconel 601 < Inconel 690. Specifically, at 288 h, the weight losses of the Inconel 601 and 690 specimens were approximately four and twelve times higher, respectively, than that of the Inconel 600 specimen. The weight loss and attack depth depended on the morphology and structure of the scale in contact with the molten salt, as well as the cracks and pores formed and the extent of Cr depletion. The corrosion products of all the tested alloys were Cr_2O_3, NiO, and $FeCr_2O_4$. The internal corrosion layer of the Inconel 600 specimen showed localized corrosion while that of the Inconel 601 and 690 specimens showed uniform corrosion. A continuous and dense external corrosion layer and a Ni-rich phase retarded the progress of the corrosion reactions, whereas a corrosion layer with high degrees of Cr and Fe depletion accelerated corrosion and caused the spallation of the protective oxide layer because of the penetration of the molten salts and oxygen through the cracks in the corrosion layer. Thus, the corrosion resistance of the Inconel alloys tested in the hot lithium molten salts in an oxidizing atmosphere is closely related to the contents of the major alloying elements in the alloys. Inconel 600 exhibited the highest corrosion resistance. Therefore, it can be concluded that the Cr content should not exceed 16.30 wt%, Ni content should not be lower than 73.66 wt%, and Fe content should be lower than 8.15 wt% to ensure improved corrosion resistance.

Author contributions KSL: Conceptualization, Formal analysis, Investigation, Methodology, Validation, Visualization, Draft preparation. WSC: Software, Methodology. WBK: Investigation, Validation. SHC: Conceptualization, Data curation, JHL: Conceptualization, Supervision, Data Curation, Project administration. All authors have read and agreed to the published version of the manuscript.

Declarations

Conflict of interest The authors have no competing interests to disclose that are relevant to this article.

References

1. A. Rehman, M. H. Bidabadi, Y. Liang, et al., *Corrosion Science* **165**, 108369 (2020). https://doi.org/10.1016/j.corsci.2019.108369.
2. A. G. Fernández and L. F. Cabeza, *Journal of Energy Storage* **229**, 101381 (2020). https://doi.org/10.1016/j.est.2020.101381.
3. Y. Grosu, A. Anagnostopoulos, M. E. Navarro, Y. Ding, and A. Faik, *Solar Energy Materials and Solar Cells* **215**, 110650 (2020). https://doi.org/10.1016/j.solmat.2020.110650.

4. A. Ruh and M. Spiegel, *Corrosion Science* **48**, 679 (2006). https://doi.org/10.1016/j.corsci.2005.02.015.
5. G. Z. Chen and D. J. Fray, *TW Nature* **407**, 361 (2000). https://doi.org/10.1038/35030069.
6. J. E. Indacochea, J. L. Smith, K. R. Litko, E. J. Karell, and A. G. Rarez, *Oxidation of Metals* **55**, 1 (2001). https://doi.org/10.1023/A:1010333407304.
7. M. Lee, C. W. Lee, H. C. Ham, J. Han, S. P. Yoon, and K. B. Lee, *International Journal of Hydrogen Energy* **42**, 16235 (2017). https://doi.org/10.1016/j.ijhydene.2017.03.096.
8. S. A. Song, H. T. Kim, K. Kim, S. N. Lim, S. P. Yoon, and S. C. Jang, *International Journal of Hydrogen Energy* **44**, 12085 (2019). https://doi.org/10.1016/j.ijhydene.2019.03.080.
9. F. Sher, N. K. Al-Shara, S. Z. Iqbal, Z. Jahan, and G. Z. Chen, *International Journal of Hydrogen Energy* **45**, 28260 (2020). https://doi.org/10.1016/j.ijhydene.2020.07.183.
10. S. W. McAlpine, N. C. Skowronski, W. Zhou, G. T. Zheng, and M. P. Short, *Journal of Nuclear Materials* **532**, 151994 (2020). https://doi.org/10.1016/j.jnucmat.2020.151994.
11. Q. Liu, Z. Wang, W. Liu, H. Yin, Z. Tang, and Y. Qian, *Corrosion Science* **180**, 109183 (2021). https://doi.org/10.1016/j.corsci.2020.109183.
12. M. A. Uusitalo, P. M. Vuoristo, and T. A. Mäntylä, *Corrosion Science* **46**, 1311 (2004). https://doi.org/10.1016/j.corsci.2003.09.026.
13. W. B. Kim, S. C. Kwon, S. H. Cho, and J. H. Lee, *Corrosion Science.* **170**, 108664 (2020). https://doi.org/10.1016/j.corsci.2020.108664.
14. D. A. Shores and B. P. Mohanty, *Corrosion Science* **46**, 2909 (2004). https://doi.org/10.1016/j.corsci.2004.04.013.
15. G. Lei, C. Li, Z. Jiang, and H. Huang, *Corrosion Science* **165**, 108408 (2020). https://doi.org/10.1016/j.corsci.2019.108408.
16. Y. Wu, B. Leng, X. Li, L. Jiang, X. Ye, Y. Chen, X. Yang, Z. Li, and X. Zhou, *Journal of Nuclear Materials* **542**, 152529 (2020). https://doi.org/10.1016/j.jnucmat.2020.152529.
17. W. H. Doniger, C. Falconer, M. Elbakhshwan, K. Britsch, A. Couet, and K. Sridharan, *Corrosion Science* **174**, 108823 (2020). https://doi.org/10.1016/j.corsci.2020.108823.
18. B. U. Yoo, S. C. Kwon, S. H. Cho, H. H. Nersisyan, and J. H. Lee, *Journal of Alloys and Compounds* **771**, 924 (2019). https://doi.org/10.1016/j.jallcom.2018.09.001.
19. X. Zhuang, W. Liu, and X. Xu, *Solar Energy* **189**, 254 (2019). https://doi.org/10.1016/j.solener.2019.07.065.
20. B. Zhu and G. Lindbergh, *Electrochimica Acta* **46**, 2593 (2001). https://doi.org/10.1016/S0013-4686(01)00471-6.
21. M. Spiegel, P. Biedenkopf, and H. J. Grabke, *Corrosion Science* **39**, 1193 (1997). https://doi.org/10.1016/S0010-938X(97)00020-6.
22. T. Tz, *Materials Chemistry and Physics* **87**, 201 (2004). https://doi.org/10.1016/j.matchemphys.2004.05.039.
23. S. Mitsushima, N. Kamiya, and K. I. Ota, *Journal of the Electrochemical Society* **137**, 2713 (1990). https://doi.org/10.1149/1.2087031.
24. X. Yang, L. Yang, J. Wang, Z. Chen, M. Chen, J. Zhang, and F. Wang, *Corrosion Science* **221**, 111377 (2023). https://doi.org/10.1016/j.corsci.2023.111377.
25. S. K. Gill, J. Sure, Y. Wang, B. Layne, L. He, S. Mahurin, J. F. Wishart, and K. Sasaki, *Corrosion Science* **179**, 109105 (2021). https://doi.org/10.1016/j.corsci.2020.109105.
26. B. Wei, C. Chen, J. Xu, L. Yang, Y. Jia, Y. Du, M. Guo, C. Sun, Z. Wang, and F. Wang, *Corrosion Science* **195**, 109996 (2022). https://doi.org/10.1016/j.corsci.2021.109996.
27. J. Feng, L. Mao, G. Yuan, Y. Zhao, J. Vidal, and L. E. Liu, *Corrosion Science* **197**, 110097 (2022). https://doi.org/10.1016/j.corsci.2022.110097.
28. Z. Xu, B. Guan, X. Wei, J. Lu, J. Ding, and W. Wang, *Solar Energy* **238**, 216 (2022). https://doi.org/10.1016/j.solener.2022.03.074.
29. X. Li, B. Leng, X. Ye, C. Liu, L. Chang, and X. Zhou, *Corrosion Science.* **194**, 109940 (2022). https://doi.org/10.1016/j.corsci.2021.109940.
30. Q. Liu, X. Liu, G. Hao, and H. Xu, *Corrosion Science* **213**, 111001 (2023). https://doi.org/10.1016/j.corsci.2023.111001.
31. H. Sun, P. Zhang, and J. Wang, *Corrosion Science* **143**, 187 (2018). https://doi.org/10.1016/j.corsci.2018.08.021.
32. X. Wang, Z. Liu, K. Cheng, Y. Shen, and J. Li, *Corrosion Science* **221**, 111308 (2023). https://doi.org/10.1016/j.corsci.2023.111308.

33. B. Meng, J. Wang, L. Yang, M. Chen, S. Zhu, and F. Wang, *Journal of Materials Science & Technology* **132**, 69 (2023). https://doi.org/10.1016/j.jmst.2022.04.054.
34. X. L. Li, S. M. He, X. T. Zhou, P. Huai, Z. J. Li, A. G. Li, and X. H. Yu, *Journal of Nuclear Materials* **464**, 342 (2015). https://doi.org/10.1016/j.jnucmat.2015.05.007.
35. T. S. Sidhu, S. Prakash, and R. D. Agrawal, *Materials Science and Engineering: A* **430**, 64 (2006). https://doi.org/10.1016/j.msea.2006.05.099.
36. J. Wang, J. Sun, B. Zou, X. Zhou, S. Dong, L. Li, J. Jiang, L. Deng, and X. Cao, *Ceramics International* **43**, 10415 (2017). https://doi.org/10.1016/j.ceramint.2017.05.077.
37. E. M. Zahrani and A. M. Alfantazi, *Corrosion Science* **85**, 60 (2014). https://doi.org/10.1016/j.corsci.2014.03.034.
38. H. Ai, X. X. Ye, L. Jiang, B. Leng, M. Shen, Z. Li, Y. Jia, J. Q. Wang, X. Zhou, Y. Xie, and L. Xie, *Corrosion Science* **149**, 218 (2019). https://doi.org/10.1016/j.corsci.2019.01.012.
39. X. Wang, L. Xin, F. Wang, S. Zhu, H. Wei, and X. Wang, *Journal of Materials Science & Technology* **30**, 867 (2014). https://doi.org/10.1016/j.jmst.2014.01.001.
40. S. Mahini, S. K. Asl, T. Rabizadeh, and H. Aghajani, *Surface and Coatings Technology* **397**, 125949 (2020). https://doi.org/10.1016/j.surfcoat.2020.125949.
41. S. H. Cho, S. S. Hong, D. S. Kang, J. M. Hur, and H. S. Lee, *Metals and Materials International* **15**, 51 (2009). https://doi.org/10.1007/s12540-009-0051-6.
42. S. H. Cho, J. M. Hur, C. S. Seo, J. S. Yoon, and S. W. Park, *Journal of Alloys and Compounds* **468**, 263 (2009). https://doi.org/10.1016/j.jallcom.2007.12.094.
43. S. H. Cho, S. C. Kwon, D. Y. Kim, W. S. Choi, Y. S. Kim, and J. H. Lee, *Corrosion Science* **151**, 20 (2019). https://doi.org/10.1016/j.corsci.2019.01.041.
44. W. B. Kim, W. S. Choi, K. S. Lim, S. H. Cho, and J. H. Lee, *Coatings* **11**, 328 (2021). https://doi.org/10.3390/coatings11030328.
45. H. Y. Woo, G. S. Lim, W. B. Kim, W. S. Choi, S. H. Cho, K. T. Park, and J. H. Lee, *Corrosion Engineering Science and Technology.* **56**, 513 (2021). https://doi.org/10.1080/1478422X.2021.1916689.
46. A. Roine, *HSC Chemistry 7.1*. (Finland: Outotec. Pori, 2018)
47. F. H. Stott, G. C. Wood, and J. Stringer, *Oxidation of Metals* **44**, 113 (1995). https://doi.org/10.1007/BF01046725.
48. H. Izuta and Y. Komura, *Journal of the Japan Institute of Metals* **58**, 1196 (1994). https://doi.org/10.2320/jinstmet1952.58.10_1196.
49. G. C. Wood, *Corrosion Science* **2**, 173 (1962). https://doi.org/10.1016/0010-938X(62)90019-7.
50. H. F. Liu, X. Xiong, X. B. Li, and Y. L. Wang, *Corrosion Science* **85**, 87 (2014). https://doi.org/10.1016/j.corsci.2014.04.001.
51. U. R. Evans, *An Introduction to Metallic Corrosion*, (Edward, London, 1948).
52. S. Ling, *Oxidation of Metals* **40**, 179 (1993). https://doi.org/10.1007/BF00665264.
53. H. M. Tawancy, *Oxidation of Metals* **45**, 323 (1996). https://doi.org/10.1007/BF01046988.
54. D. Caplan and M. Cohen, *Corrosion* **15**, 57 (1959). https://doi.org/10.5006/0010-9312-15.3.57.